Optimizing noise for defect analysis with through-focus scanning optical microscopy

Ravikiran Attota*, John Kramar
Engineering Physics Division, PML, NIST, Gaithersburg, Maryland, 20899, USA

ABSTRACT

Through-focus scanning optical microscopy (TSOM) shows promise for patterned defect analysis, but it is important to minimize total system noise. TSOM is a three-dimensional shape metrology method that can achieve sub-nanometer measurement sensitivity by analyzing sets of images acquired through-focus using a conventional optical microscope. Here we present a systematic noise-analysis study for optimizing data collection and data processing parameters for TSOM and then demonstrate how the optimized parameters affect defect analysis. We show that the best balance between signal-to-noise performance and acquisition time can be achieved by judicious spatial averaging. Correct background-signal subtraction of the imaging-system inhomogeneities is also critical, as well as careful alignment of the constituent images used in differential TSOM analysis.

Keywords: TSOM, noise optimization, defect analysis,

1. INTRODUCTION

As the use of three-dimensional (3-D) components in nanotechnology increases, high-throughput and economical 3-D shape analysis and process monitoring of nanoscale objects is increasingly desirable[1-5] and at the same time increasingly challenging [5, 6]. Several excellent metrology tools are currently available for such a purpose [7-44], with each tool having certain advantages and disadvantages. However, it would be beneficial if metrology could be done using a widely available, low cost, tool such as a conventional optical microscope. We and other researchers have shown that this can be achieved using through-focus scanning optical microscopy (TSOM) [6, 45-56]. Furthermore, the same approach can be extended to patterned defect analysis [57, 58] and also to larger microscale targets making TSOM a valuable 3-D metrology method for targets ranging from the nanoscale to the microscale.

Application of TSOM has been demonstrated for several metrology challenges including, but not limited to: critical dimension (linewidth), overlay, patterned defect detection and analysis, FinFETs, nanoparticles, photo-mask linewidth, thin-film thickness, through-silicon vias (TSVs), high-aspect-ratio (HAR) targets and others [6, 45-55]. Though not yet published, we have also shown the applicability of TSOM for fabrication process monitoring of MEMS/NEMS devices and micro/nanofluidic channels. Sub-nanometer measurement resolution has been demonstrated [6, 49]. Three-dimensional shape analysis of isolated sub-50 nm wide lines with sub-nanometer resolution was experimentally demonstrated using visible illumination wavelength of 546 nm [6]. Measurement sensitivity of less than 0.1 nm was revealed for sub-25 nm wide lines (critical dimensions (CDs)) again using 546 nm wavelength [6]. TSOM is being increasingly recognized as a viable nanometrology method, as evidenced by being listed in several technology road maps and guides [59-61], patent applications [62, 63], and science news reports [64, 65].

Given the increasing attention, it is important that we systematically address how to optimize the data collection and analysis conditions. Here we present common parameters that affect the noise and study how these parameters can be practically optimized for reduction of the noise. In this paper we deal only with the optical system noise. Wafer noise such as generated due to line edge roughness [66] is not included. The parameters under consideration are commonly known, but they are here applied uniquely to TSOM. Following this we demonstrate how the optimized parameters affect defect analysis.

---

*Ravikiran.attota@nist.gov; phone +1 301 975 5750

A typical TSOM image is a cross-section constructed from the four-dimensional (4-D) optical data [49] acquired using a conventional optical microscope as a target is scanned along the focus direction [49, 52]. A multimedia figure depicting the method for constructing a TSOM image is presented in Video. 1 [52]. In the TSOM image the X (horizontal), Y (vertical), and color scale axes represent the spatial position across the target, the focus position, and the optical intensity, respectively. A differential TSOM (D-TSOM) image is produced by subtracting two TSOM images (usually obtained from two similar targets). The D-TSOM images thus produced highlight the dimensional differences down to a sub-nanometer scale [6, 49]. In addition, the D-TSOM image patterns are distinct for different types of parameter changes, but qualitatively similar for different magnitude changes in the same parameter [48, 49].

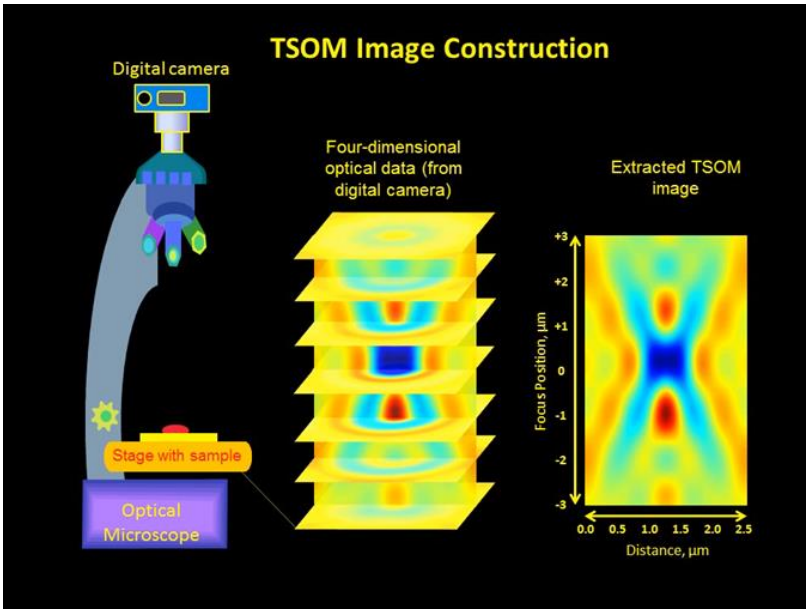

Video 1. The method for constructing a TSOM image. http://dx.doi.org/doi.number.goes.here

Optical content of a D-TSOM image provides valuable information about the 3D shape of the targets being compared, including defects. Optical content includes both the pattern created by variations in the optical signal strength and the magnitude of the optical signal itself. One of the ways to quantify the optical signal strength is by using optical intensity range (OIR), [6] defined as the absolute difference between the maximum and the minimum optical signal strength in a given TSOM image (or D-TSOM image) multiplied by 100. If the OIR of a given topographical difference (between any two targets) is safely above the noise level, then that dimensional difference can be detected with no ambiguity. However, as the magnitude of the dimensional difference decreases, there comes a point where OIR of the signal generated due to the dimensional difference is similar to or less than that of the OIR of the microscope system noise. Under these circumstances that dimensional difference cannot be detected with confidence as the signal from the noise dominates the signal from the dimensional difference. This necessitates optimal reduction, and also determination of the base level of the optical system noise. We perform this exercise in this paper.

The following method was chosen to quantify the total noise. Generate a D-TSOM image using two independently acquired and constructed TSOM images from the same target under the exact same experimental conditions. If done correctly, this process will subtract out the signal from the target and the optical signal due the presence of optical and illumination aberrations. The resultant D-TSOM image is a representation of the total system noise. It is observed that this noise is usually random in nature. The following parameters (that affect the noise) have been studied here: background signal, smoothing filter span, width of the window of analysis (explained below), camera pixels, focus step height, number of interpolation points, and optical image signal strength.

An isolated Si line (nominally 31 nm linewidth and 70 nm height) on a Si substrate was used as the target. The fabrication of the target is similar to that reported earlier [6, 49, 56]. The TSOM data were acquired using a bright-field optical microscope (Zeiss Axio Imager.Z1) in the reflection mode (focus reproducibility = ±10 nm, objective magnification = 50x, collection numerical aperture (NA) = 0.55, illumination NA = 0.157, illumination wavelength = 520 nm (narrow band-pass filtered LED light source, unpolarized, total focus range of about 25 μm)). Each analysis requires three through-focus data sets under the same experimental conditions: two datasets (essentially repeats) from the selected isolated line, and one data set from a smooth, clean Si surface. The third dataset (from the smooth Si surface) is required to remove the background signal due to the imperfections in the optical system from the two target datasets. TSOM analysis was done using software developed at NIST. The software performs the following steps to the data: normalizes each through-focus image with its own mean intensity as given in Refs. [6, 56], subtracts the through-focus background noise optical image from the target optical image at each focus-height step, selects the through-focus optical images (from the background-subtracted target image) bound by a box (as shown in Fig. 2(a)), extracts an intensity profile by averaging along the box-width "W" (Fig. 1(a)) at each focus height, constructs TSOM images by stacking the intensity profiles at their respective focus positions, interpolates, and smoothens. The normalization process (first step) eliminates the effect of overall image intensity variations, if present. The two processed TSOM images obtained in this way are then cross-correlated in both horizontal and vertical directions to achieve the best aligned position. They are then subtracted to obtain D-TSOM images. This process is shown as a flow chart in Fig.1.

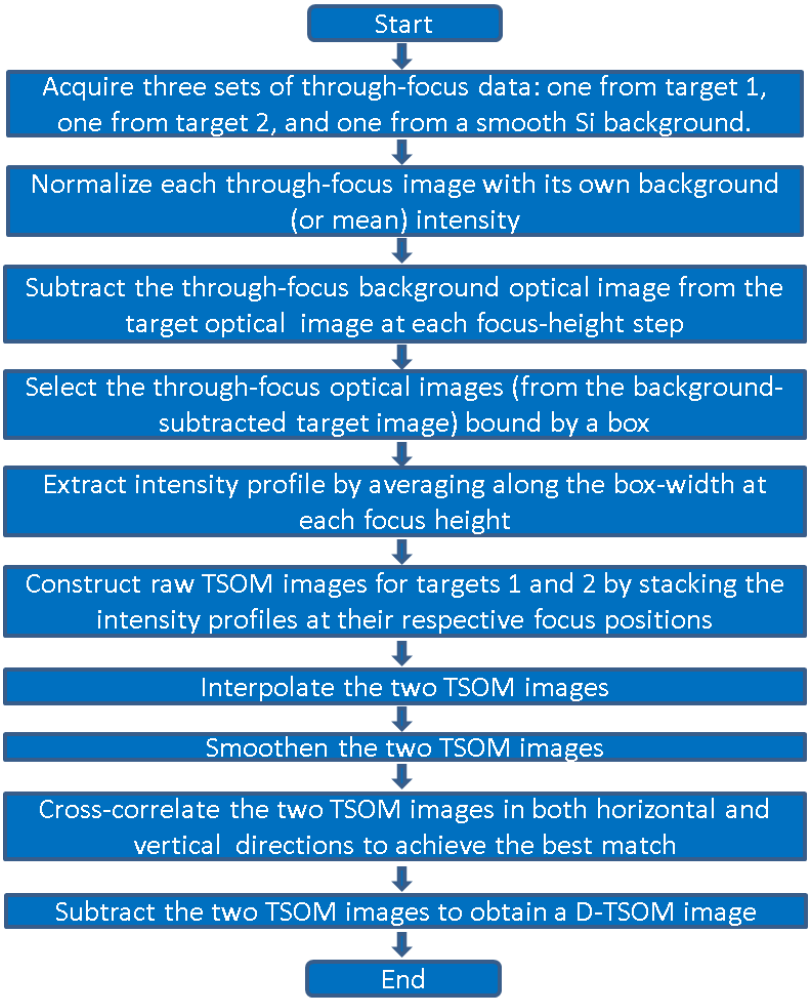

Fig. 1. Flow chart showing the steps to obtain a D-TSOM image. In this case the targets 1 and 2 are the same (repeats) and hence the D-TSOM image will be a noise D-TSOM image.

We have arrived at the following optimized conditions (or processes) for our current experimental setup based on the noise analysis and practical limitations [56]: background signal must be subtracted, box-width for analysis W = 1 μm, camera pixels = 694x520 (65 nm/pixel), focus step height = 300 nm, interpolated pixel size = 20 nm/pixel, smoothing filter span = 400 nm, and mean optical image signal strength = 100 A.U. (Arbitrary Unit). Of course, some variation in the optimized parameter values is likely depending on the specific experimental setup, measurement needs and personal judgement. In the following paragraphs we study the individual effect of each parameter on the noise by keeping the other parameters fixed. The OIR values provided are averages from 5 independent measurements. Mean OIR Standard deviations of all the TSOM images and all the D-TSOM images calculated for this study are about 1.4 % and 9 %, respectively.

Background signal removal has a profound effect on the TSOM image noise. In Figs. 2(a) and (b) we show optical images at approximately the best focus position for the target and for the smooth Si surface (which serves as the background signal image), respectively. No dramatic change can be observed in the background image subtracted target image (Fig. 2(c)), except for a change in the optical intensity scale. However, a dramatic change can be observed in the TSOM image after performing this operation. Raw TSOM images of the target (Fig. 2(d)) and the background signal (Fig. 2(e)) show background signal (or microscope noise) as streaks running from top to bottom. These streaks are completely removed in the background signal subtracted raw TSOM image (Fig. 2(f)). The subsequent image processing steps performed on the raw TSOM image remove pixelation (Fig. 2(g)). However, they also result in a loss in OIR (i.e. optical signal strength, which is essentially the absolute range of the color scale bar on the right side of the image) from 21.5 to 12.3. But this process is necessary for a meaningful analysis. Any method that satisfactorily removes pixelation can be adopted. Variations in the optical intensity profiles at the different focus positions (Fig. 2(h)) and relative orientations of the optical image plane with respect to the TSOM image plane (Fig. 2(i)) are provided for better visualization of the TSOM images.

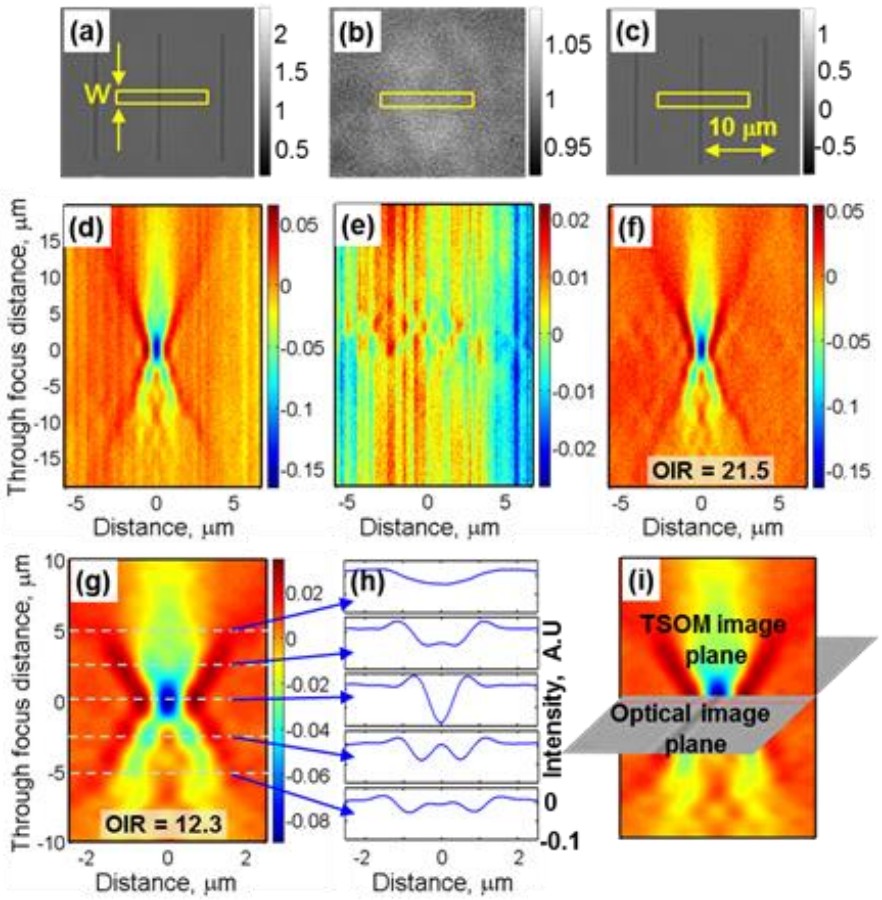

Fig. 2. Raw optical images of (a) the target, (b) a smooth Si surface, which serves as the background signal, and (c) the background-signal-subtracted target. The box shows the area selected for analysis. Raw TSOM images of (d) the target, (e) the background signal and (f) the background-signal-subtracted target. (g) The processed TSOM image. (h) Intensity profiles at the dotted lines shown in (g), and (i) optical and TSOM image planes showing their relative orientations.

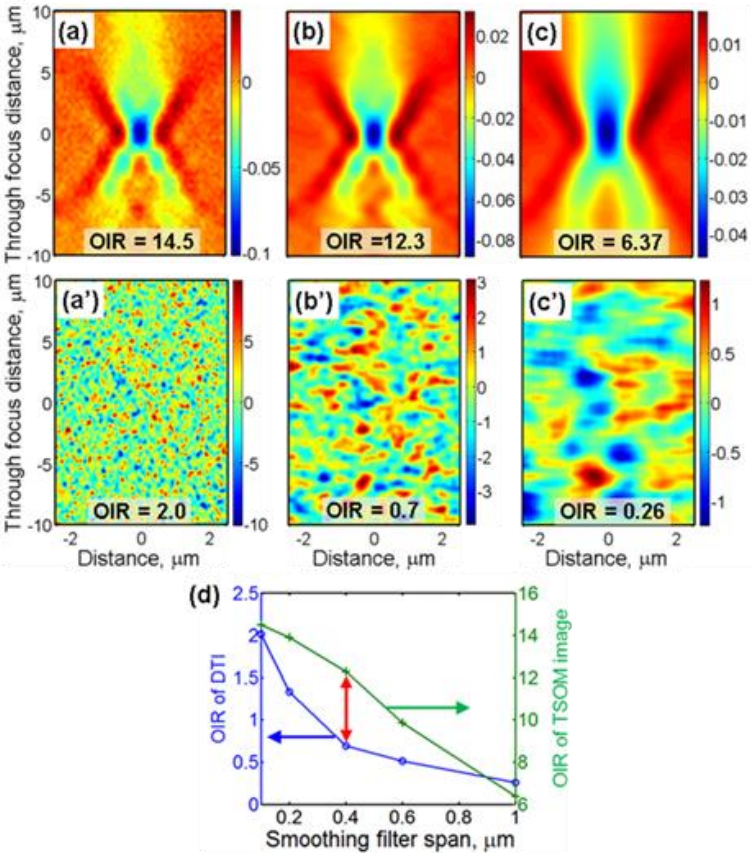

Fig. 3. (a), (b), and (c) TSOM images; and (a'), (b'), and (c') the D-TSOM images showing noise for spans of 0.1 µm, 0.4 µm, and 1.0 µm, respectively. (d) A summary plot showing the effect of moving-average span on OIRs of the TSOM images and the noise D-TSOM images as a function of the smoothing filter span. The red double arrow indicates the span selected.

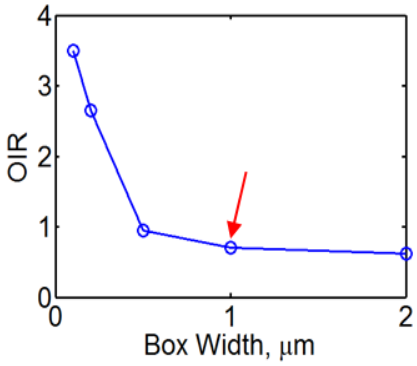

Fig. 4. Effect of the box-width 'W' (Fig. 2(a)) on the noise OIR. The red arrows indicate the selected optimized values.

Smoothing the intensity profiles is a critical step for reducing noise. Even though there are several possible smoothing methods, to demonstrate the process we here apply the moving-average method independently both in the horizontal and the vertical directions. The span of the moving-average is the variable that needs to be optimized. The span determines the number of points (or pixels) over which the averaging is performed. Initial smoothing was performed at half the nominal span length first in the horizontal direction followed by in the vertical direction. In the second step the same process was repeated at the full span length, completing the smoothing process. Smoothing significantly affects the OIR and also the noise. The TSOM image that is not smoothed shows a high OIR, but at the same time has excess pixel noise (Fig. 3 (f)), which interferes with repeatable analysis. A small span length of 0.1 µm still results in a pixelated TSOM image (Fig. 3(a)), even though the OIR decreases significantly from 21.5 to 14.5. The D-TSOM image showing noise has a large OIR of 2.0 (Fig. 3(a')). A four-fold increase in the span length from 0.1 µm to 0.4 µm reduces the OIR of the TSOM image by a small amount (from 14.5 to 12.3, Fig. 3(b)), but it significantly reduces the noise OIR from 2.0 to 0.7 (Fig. 3(b')). Further increase in the span length to 1.0 µm significantly distorts the TSOM image (Fig. 3(c)) and hence is over smoothed for most purposes, even though the noise OIR has a further reduced value of 0.26 (Fig. 3(c')). A summary of these results is plotted in Fig. 3(d). The goal here is to maximize the TSOM image signal strength (i.e., the OIR of the TSOM image) and minimize the noise (i.e., the OIR of the noise D-TSOM image) while at the same time minimizing distortion in the TSOM image. We aim to get a noise OIR of less than 1. In the current study, a span length of 0.4 µm satisfies these conditions, and hence it was selected as the optimized span length.

It is important to note that in the D-TSOM images (Figs. 3(a'), (b'), and (c')) no residual optical signal from the line can be detected. They appear to be dominated by purely noise indicating that the other parameters selected and cross-correlation performed to obtain the D-TSOM images are well-chosen.

We turn now to the effect of box-width "W" (as shown in Fig. 2(a)), which is related to the number of profiles that are averaged to get a mean intensity profile. In Fig. 4 we plot the effect of box width on the noise OIR. As expected, smaller widths result in higher noise. The plot shows that widths

in the range of 0.5 μm to 2 μm provide a noise OIR of less than 1. From this range we chose 1 μm, but it could also be 0.5 μm.

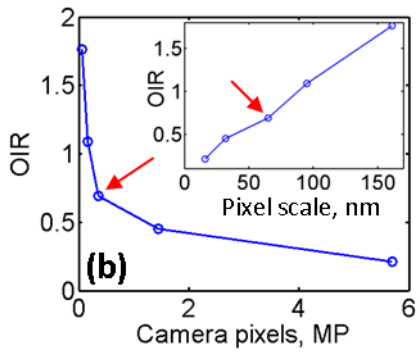

Fig. 5. Effect of the camera pixels on the noise OIR. The inset shows the same data plotted as a function of pixel scale. The red arrows indicate the selected optimized values.

The digital monochrome camera used has a native pixel count of 1040x1388 (1.44 MP). Under the magnifications used, this results in a scale of 32 nm/pixel in the digital image. Different pixel counts (pixel scale) can be achieved by pixel-binning which has two opposing effects. Binning increases signal-to-noise ratio of cameras, but it also reduces image resolution (reduces pixel count). For image analysis the former is beneficial, but the latter is detrimental. In this study we varied the illumination source intensity to maintain the image signal strength at the same level for the different pixel-binning levels selected. In this way we could study only the effect of pixel count on the noise. Different pixel counts of 208x276 (0.057 MP, 161 nm/pixel), 346x462 (0.16 MP, 95 nm/pixel) and 520x694 (0.36 MP, 65 nm/pixel) were achieved by pixel-binning. A large pixel count of 2080x2776 (5.7 MP, 16 nm/pixel) was also obtained by using the CCD sensor's piezo-scanning feature of the camera. OIR of the noise plotted as a function of the pixel count shows a continuous decrease in the noise OIR with increased pixel count (Fig. 5). The same data plotted as a function of the pixel scale (inset of Fig. 5) shows a nearly linear decreasing trend in the noise OIR with the decreasing pixel scale. This clearly demonstrates the benefit of using high pixel count in reducing the noise. Based on the less-than-1 noise OIR criteria we chose the 520x694 pixel count which produces a noise OIR of 0.7. However, if the noise needs to be reduced further, a higher pixel count could be selected (for example 2080x2776 pixels). But in this case it would require 16 times more disk storage space compared to 520x694 pixel count and also has a disadvantage of slower processing of the data. Practical feasibility also needs to be considered in selecting the optimum pixel count.

Interpolation can be used as a means of artificially increasing the pixel count. In the above pixel count study, an interpolated pixel scale (using spline method) of approximately 20 nm/pixel was maintained irrespective of the image pixel count (except for the 2080x2776 pixel count where it was 16 nm/pixel). Here we present the effect of varying interpolated pixel scale for the 520x694 pixel count (65 nm/pixel). A plot of the noise OIR as a function of the interpolated pixel scale also shows a decreasing trend in the noise with decreasing interpolated pixel size (Fig. 6(a)). From this we chose a 20 nm pixel size (shown by an arrow in Fig 6(a)). This results in a smooth TSOM image and a noise OIR much less than 1 (Figs. 3(b) and 3(b')). Technically we could choose 32 nm/pixel scale also as it results in a noise OIR less than 1. However, a larger interpolated pixel size has undesirable effect of residual intensity (color pattern) in the D-TSOM images. For example, at 65 nm/pixel scale (no interpolation) a residual color pattern in the D-TSOM image can be clearly seen as highlighted by a circle in Fig. 6(b). This is due to imperfect alignment for cross-correlation that is limited by the large pixel size. Any pixel size (either original or interpolated) that produces a residual color pattern should be avoided as much as possible. The interpolation primarily has the benefit of decreasing noise while using larger-pixel-size images (smaller stored image sizes). However, the reduction in noise is not as good as acquiring images directly at a smaller pixel scale. For example, images acquired directly at 16 nm/pixel scale show a noise OIR of 0.21 (from Fig. 5), while at the similar interpolated pixel scale noise OIR has a value of about 0.65 (from Fig. 6(a)), which is nearly three times the former. At the same time the interpolation has the benefit of reducing the noise OIR from 1.03 to 0.55 (Fig. 6(a))).

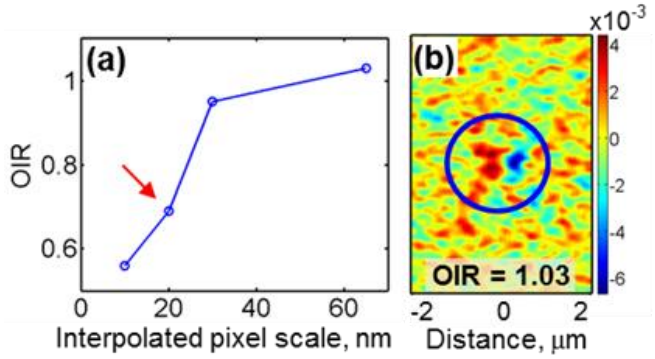

Fig. 6 (a) Effect of the interpolated pixel scale on the noise OIR. (b) A D-TSOM image showing the residual optical content (highlighted by a circle) due to imperfect cross-correlation as a result of a large scale of 65 nm/pixel.

Optical image signal strength also has a strong influence on the noise level. Under a given set of experimental conditions, a combination of illumination source intensity and the camera exposure time determines the image signal strength. Here we varied the camera exposure time to obtain the different image signal strengths. Mean image signal strength was calculated from the set of through-focus images obtained using a smooth Si background surface. The data presented here was collected at a higher source intensity compared to the other data presented earlier. As shown in Fig. 7, noise OIR decreases with increased image signal strength. This suggests that higher image signal strengths are desirable to reduce the noise level.

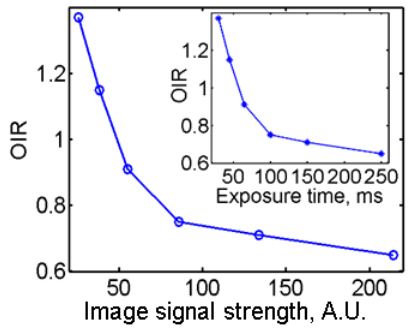

Fig. 7 Effect of the optical image signal strength on the noise OIR. The inset shows the same data as a function of the camera exposure time.

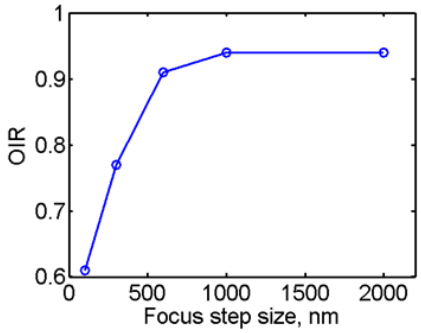

Fig. 8. Effect of the focus-step size on the noise OIR.

Similar to pixel scale (Fig. 3), focus-step size shows increased noise with increased step size as shown in Fig. 8. However, unlike pixel scale, the noise tapers out above 1000 nm step size under the current experimental conditions (this data was collected at a mean Si background image irradiance of 90 A.U.). As far as noise is concerned, any step size results in below 1 noise OIR. However, D-TSOM images appear distorted for larger step sizes and hence we chose a step size of 300 nm.

As an example, here we present the effect of optimizing parameters on the detectability of a patterned defect. To demonstrate this, we selected a 7 nm, Type-A patterned defect as shown in Fig. 9(a). Optical simulations show that this patterned defect has an OIR (or the defect signal strength) of 1.8 as shown in Fig. 9(b) [58, 67]. We need noise signal at λ = 246 nm (where the optical simulations were obtained) to demonstrate the effect of noise. However, at present we do not have access to it. As a compromise, we created different-magnitude experimental noise at λ = 520 nm using box-width as the parameter, and used this noise for defect detectability test. Box-width values of 2.0 μm and 0.4 μm produced low and high noise OIRs of 0.8 and 1.9, respectively (Figs. 9(c) and 9(d)). Adding the experimentally obtained noises (Figs. 9(c) and 9(d)) to the simulated noise-less defect signal (Fig. 9(b)) results in Figs. 9(e) and 9(f), demonstrating the effect of (artificial) noise on the defect detectability. The defect has a much better chance of detectability with a low noise (Fig. 9(e)) as we can still observe the characteristic defect pattern. On the other hand, a high noise signal makes it much harder to detect the defect (Fig. 9(f)). This demonstrates the importance of reducing the TSOM and D-TSOM image noise by optimizing the acquisition and data processing parameters so that the limits of defect detection can be extended to smaller size defects.

In summary, we have here presented the steps we typically use to process through-focus optical data for the TSOM method of analysis. We have also demonstrated practical ways to reduce noise while retaining the key information. We have studied the effect of parameters such as background signal, smoothing filter span, width of the window of analysis, camera-pixel size, focus-step height, number of interpolation points, and optical image signal strength on the noise signal strength (OIR). The parameters can be adjusted to suit individual needs, but the values provided here can serve as a guide for a starting point. For a new type of sample or analysis, or under a new set of conditions, we usually strive to achieve a noise OIR of less than 1. It is wise to perform the noise test often to monitor the continued integrity of the measurement and analysis process.

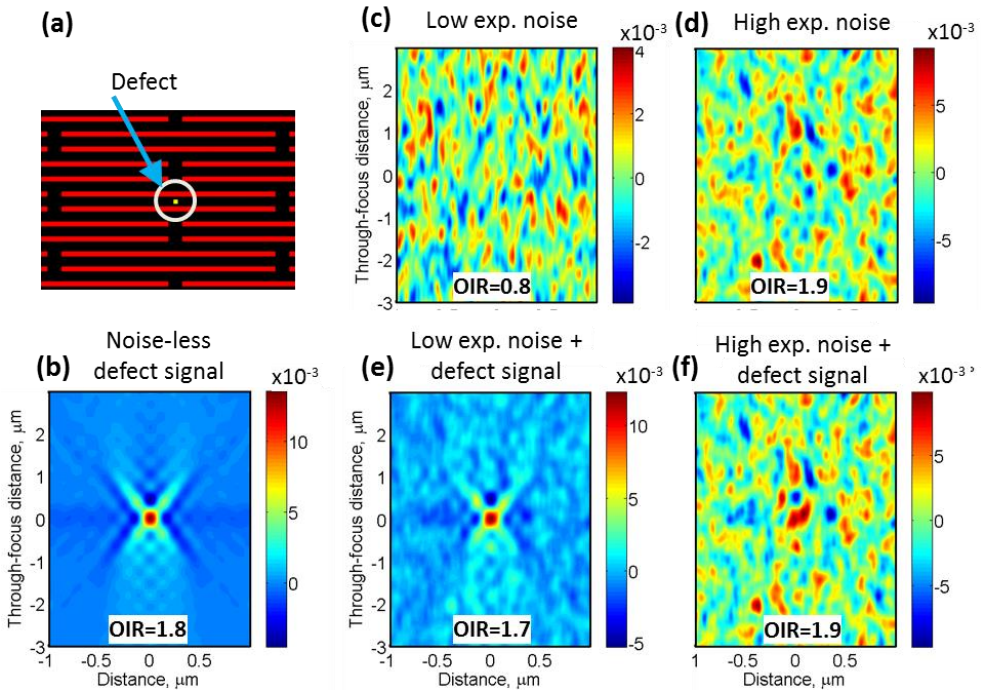

Fig. 9. (a) Type A patterned defect (defect size = 7 nm, CD = 7 nm, Pitch = 21 nm, λ = 248 nm, Si material). (b) Simulated noise-less, D-TSOM image of the defect in (a). (c) Low-noise obtained experimentally using a box-width of 1.9 µm. (d) High-noise obtained experimentally using a box-width of 0.4 µm. (e) Combined noise-less defect signal with low-noise. (f) Combined noise-less defect signal with high-noise.

Disclaimer: Any mention of commercial products or entities in this paper is for informational purposes only; it does not imply recommendation or endorsement by NIST.

Acknowledgement: The author would like to thank Richard Kasica of CNST, for providing the sample.

REFERENCES

[1] G. B. Picotto, L. Koenders, and G. Wilkening, "Nanoscale metrology," Measurement Science and Technology, 20(8), 080101 (2009).

[2] G. Häusler, and S. Ettl, [Limitations of Optical 3D Sensors] Springer Berlin Heidelberg, 3 (2011).

[3] K. L. Richard, B. Robert, B. Theresa *et al.*, "The European nanometrology landscape," Nanotechnology, 22(6), 062001 (2011).

[4] G. Berkovic, and E. Shafir, "Optical methods for distance and displacement measurements," Advances in Optics and Photonics, 4(4), 441-471 (2012).

[5] A. Vaid, A. Elia, G. Iddawela *et al.*, "Hybrid metrology: from the lab into the fab," Journal of Micro/Nanolithography, MEMS, and MOEMS, 13(4), 041410-041410 (2014).

[6] R. Attota, B. Bunday, and V. Vartanian, "Critical dimension metrology by through-focus scanning optical microscopy beyond the 22 nm node," Applied Physics Letters, 102(22), (2013).

[7] H. Schroettner, M. Schmied, and S. Scherer, "Comparison of 3D surface reconstruction data from certified depth standards obtained by SEM and an infinite focus measurement machine (IFM)," Microchimica Acta, 155(1), 279-284 (2006).

[8] C. Wang, R. L. Jones, E. K. Lin *et al.*, "Small angle x-ray scattering measurements of lithographic patterns with sidewall roughness from vertical standing waves," Applied Physics Letters, 90(19), 193122 (2007).
[9] T. M. Bao, L. Mininni, and D. Dawson, "Improving Sidewall Profile Metrology with Enhanced 3D-AFM," Lithography Asia 2008, 7140, (2008).
[10] J. A. Kramar, R. Dixson, and N. G. Orji, "Scanning probe microscope dimensional metrology at NIST," Measurement Science & Technology, 22(2), (2011).
[11] N. G. Orji, R. G. Dixson, A. E. Vladar *et al.*, "Strategies for Nanoscale Contour Metrology using Critical Dimension Atomic Force Microscopy," Proceedings of SPIE, 8105, 810505 (2011).
[12] J. Carrero, and G. Percin, "Accurate Optical CD Profiler Based On Specialized Finite Element Method," Proceedings of SPIE, 8324, 83240P (2012).
[13] G. L. Dai, W. Hassler-Grohne, D. Huser *et al.*, "New developments at Physikalisch Technische Bundesanstalt in three-dimensional atomic force microscopy with tapping and torsion atomic force microscopy mode and vector approach probing strategy," Journal of Micro-Nanolithography Mems and Moems, 11(1), (2012).
[14] A. E. Vladar, P. Cizmar, J. S. Villarrubia *et al.*, "Can We Get 3D CD Metrology Right?," Proceedings of SPIE, 8324, 832402 (2012).
[15] H. Chouaib, and Q. Zhao, "Nanoscale optical critical dimension measurement of a contact hole using deep ultraviolet spectroscopic ellipsometry," Journal of Vacuum Science & Technology B, 31(1), (2013).
[16] J. Li, O. Kritsun, P. Dasari *et al.*, "Evaluating Scatterometry 3D Capabilities for EUV," Proceedings of SPIE, 8681, 86810S (2013).
[17] J. Qin, R. M. Silver, B. M. Barnes *et al.*, "Fourier domain optical tool normalization for quantitative parametric image reconstruction," Applied Optics, 52(26), 6512-6522 (2013).
[18] D. F. Sunday, M. R. Hammond, C. Q. Wang *et al.*, "Three-dimensional x-ray metrology for block copolymer lithography line-space patterns," Journal of Micro-Nanolithography Mems and Moems, 12(3), (2013).
[19] A. Yamaguchi, T. Ohashi, T. Kawasaki *et al.*, "Three-dimensional profile extraction from CD-SEM image and top/bottom CD measurement by line-edge roughness analysis," Proceedings of SPIE, 8681, 86812Z (2013).
[20] R. Chao, K. K. Kohli, Y. L. Zhang *et al.*, "Multitechnique metrology methods for evaluating pitch walking in 14 nm and beyond FinFETs," Journal of Micro-Nanolithography Mems and Moems, 13(4), (2014).
[21] Y. S. Ku, "Spectral reflectometry for metrology of three-dimensional through-silicon vias," Journal of Micro-Nanolithography Mems and Moems, 13(1), (2014).
[22] R. M. Silver, B. M. Barnes, N. F. Zhang *et al.*, "Optimizing Hybrid Metrology through a Consistent Multi-Tool Parameter Set and Uncertainty Model," Proceedings of SPIE, 9050, 905004 (2014).
[23] A. Vaid, C. Osorio, J. Tsai *et al.*, "Hybrid metrology universal engine: co-optimization," Proceedings of SPIE, 9050, 905009 (2014).
[24] A. E. Vladar, J. S. Villarrubia, J. Chawla *et al.*, "10 nm Three-Dimensional CD-SEM Metrology," Proceedings of SPIE, 9050, 90500A (2014).
[25] X. X. Zhang, H. Zhou, Z. H. Ge *et al.*, "Addressing FinFET metrology challenges in 1x node using tilt-beam critical dimension scanning electron microscope," Journal of Micro-Nanolithography Mems and Moems, 13(4), (2014).
[26] X. X. Zhang, P. Snow, A. Vaid *et al.*, "Solving next generation (1X node) metrology challenges using advanced CDSEM capabilities: tilt, high energy and backscatter imaging," Proceedings of SPIE, 9424, 94240G (2015).
[27] Y.-M. Lee, J.-H. Li, P. C. W. Ng *et al.*, "Efficient scattering simulations for equivalent extreme ultraviolet mask multilayer structures by modified transmission line theory and finite-difference time-domain method," Journal of Micro/Nanolithography, MEMS, and MOEMS, 9(4), 043003-043003-15 (2010).
[28] T. F. Crimmins, "Wafer noise models for defect inspection." 7971, 79710E-79710E-6.
[29] A. Vaid, B. B. Yan, Y. T. Jiang *et al.*, "Holistic metrology approach: hybrid metrology utilizing scatterometry, critical dimension-atomic force microscope and critical dimension-scanning electron microscope," Journal of Micro/Nanolithography, MEMS, and MOEMS, 10(4), 043016-043016-13 (2011).
[30] J. Ahn, B. Lee, D.-R. Lee *et al.*, "Optical analysis on the wafer defect inspection for yield enhancement." 8681, 86811E-86811E-7.
[31] S. Godny, M. Asano, A. Kawamoto *et al.*, "Hybrid approach to optical CD metrology of directed self-assembly lithography." 8681, 86812D-86812D-8.
[32] C. J. Raymond, and Z. Li, "Photoluminescence metrology for LED characterization in high volume manufacturing." 8681, 86810P-86810P-8.

[33] J. P. Cain, N. P. Rodriguez, J. Sweis *et al.*, "A pattern-driven design regularization methodology." 9053, 905303-905303-9.
[34] K.-H. Chen, G. T. Huang, K. S. Chen *et al.*, "Improving on-product performance at litho using integrated diffraction-based metrology and computationally designed device-like targets fit for advanced technologies (incl. FinFET)." 9050, 90500S-90500S-10.
[35] K. Hitomi, S. Halle, M. Miller *et al.*, "Hybrid OPC modeling with SEM contour technique for 10nm node process." 9052, 90520W-90520W-9.
[36] Y.-S. Ku, "Spectral reflectometry for metrology of three-dimensional through-silicon vias," Journal of Micro/Nanolithography, MEMS, and MOEMS, 13(1), 011209-011209 (2014).
[37] X. Zhang, H. Zhou, Z. Ge *et al.*, "Addressing FinFET metrology challenges in 1× node using tilt-beam critical dimension scanning electron microscope," Journal of Micro/Nanolithography, MEMS, and MOEMS, 13(4), 041407-041407 (2014).
[38] R. Chao, C.-C. Liu, C. Bozdog *et al.*, "Scatterometry-based defect detection for DSA in-line process control." 9424, 942419-942419-17.
[39] M.-A. Henn, R. M. Silver, J. S. Villarrubia *et al.*, "Optimizing hybrid metrology: rigorous implementation of Bayesian and combined regression," Journal of Micro/Nanolithography, MEMS, and MOEMS, 14(4), 044001-044001 (2015).
[40] A. Starikov, and M. Sendelbach, "Special Section Guest Editorial: Control of IC Patterning Variance Part 1: Metrology, Process Monitoring, and Control of Critical Dimension," Journal of Micro/Nanolithography, MEMS, and MOEMS, 14(2), 021101-021101 (2015).
[41] L. Subramany, W. J. Chung, K. Gutjahr *et al.*, "HVM capabilities of CPE run-to-run overlay control." 9424, 94241V-94241V-7.
[42] A. Vaid, G. Iddawela, J. Tsai *et al.*, "Improved scatterometry time-to-solution using virtual reference." 9424, 94240X-94240X-9.
[43] X. Zhang, P. W. Snow, A. Vaid *et al.*, "Solving next generation (1x node) metrology challenges using advanced CDSEM capabilities: tilt, high energy and backscatter imaging." 9424, 94240G-94240G-14.
[44] R. Attota, R. M. Silver, M. Stocker *et al.*, "A new method to enhance overlay tool performance," Metrology, Inspection, and Process Control for Microlithography Xvii, Pts 1 and 2, 5038, 428-436 (2003).
[45] R. Attota, R. M. Silver, and J. Potzick, "Optical illumination and critical dimension analysis using the through-focus focus metric method - art. no. 62890Q," Novel Optical Systems Design and Optimization IX, 6289, Q2890-Q2890 (2006).
[46] R. Attota, T. A. Germer, and R. M. Silver, "Through-focus scanning-optical-microscope imaging method for nanoscale dimensional analysis," Optics Letters, 33(17), 1990-1992 (2008).
[47] R. Attota, R. G. Dixson, J. A. Kramar *et al.*, "TSOM Method for Semiconductor Metrology," Metrology, Inspection, and Process Control for Microlithography Xxv, Pt 1 and Pt 2, 7971, (2011).
[48] R. Attota, and R. Silver, "Nanometrology using a through-focus scanning optical microscopy method," Measurement Science & Technology, 22(2), (2011).
[49] R. Attota, and R. G. Dixson, "Resolving three-dimensional shape of sub-50 nm wide lines with nanometer-scale sensitivity using conventional optical microscopes," Applied Physics Letters, 105(4), (2014).
[50] M. V. Ryabko, S. N. Koptyaev, A. V. Shcherbakov *et al.*, "Method for optical inspection of nanoscale objects based upon analysis of their defocused images and features of its practical implementation," Optics Express, 21(21), 24483-24489 (2013).
[51] S. Usha, Shashikumar, P.V., Mohankumar, G.C., Rao, S.S., "Through Focus Optical Imaging Technique To Analyze Variations In Nano-Scale Indents," International Journal of Engineering Research & Technology, 2(5), 18 (2013).
[52] R. Attota, P. P. Kavuri, H. Kang *et al.*, "Nanoparticle size determination using optical microscopes," Applied Physics Letters, 105(16), (2014).
[53] M. Ryabko, S. Koptyaev, A. Shcherbakov *et al.*, "Motion-free all optical inspection system for nanoscale topology control," Optics Express, 22(12), 14958-14963 (2014).
[54] A. L. Balk, L. O. Mair, F. Guo *et al.*, "Quantitative magnetometry of ferromagnetic nanorods by microfluidic analytical magnetophoresis," Journal of Applied Physics, 118(9), (2015).
[55] M. Ryabko, A. Shchekin, S. Koptyaev *et al.*, "Through-focus scanning optical microscopy (TSOM) considering optical aberrations: practical implementation," Optics Express, 23(25), 32215-32221 (2015).
[56] R. Attota, "Noise analysis for through-focus scanning optical microscopy," Optics Letters, 41(4), (2016).

[57] A. Arceo, B. Bunday, V. Vartanian *et al.*, "Patterned Defect & CD Metrology by TSOM Beyond the 22 nm Node," Proc. of SPIE, 8324, 83240E (2012).
[58] A. Arceo, B. Bunday, and R. Attota, "Use of TSOM for sub-11 nm node pattern defect detection and HAR features," Proc. of SPIE, 8681, 86812G (2013).
[59] S. I. Association, [The International Technology Roadmap for Semiconductors (ITRS)] Semiconductor Industry Association, San Jose(2011).
[60] B. Bunday, T. A. Germer, V. Vartanian *et al.*, "Gaps Analysis for CD Metrology Beyond the 22 nm Node," Metrology, Inspection, and Process Control for Microlithography Xxvii, 8681, (2013).
[61] S. E. M. I. document, [Guide for metrology techniques to be used in measurement of geometrical parameters of through- silicon vias (TSVs) in 3DS-IC structures] SEMI, (2013).
[62] S. N. KOPTYAEV, KOPTYAEV, S.N., RYABKO, M.V., Rychagov, M.N, [Optical measurement system and method for measuring critical dimension of nanostructure], USA(2013).
[63] S. N. KOPTYAEV, RYABKO, M.V., HCHERBAKOV, A.V., LANTSOV, A.D., [Optical measuring system and method of measuring critical size], USA(2014).
[64] R. Attota, Jindal, V., "Inspecting mask defects with through-focus scanning optical microscopy,", SPIE Newsroom, (2013).
[65] M. Ryabko, Koptyev, S., Shchekin, A., Medvedev, A., "Improved critical dimension inspection for the semiconductor industry," SPIE Newsroom, (2014).
[66] B. M. Barnes, F. Goasmat, M. Y. Sohn *et al.*, "Effects of wafer noise on the detection of 20-nm defects using optical volumetric inspection," Journal of Micro-Nanolithography Mems and Moems, 14(1), (2015).
[67] A. Arceo, B. Bunday, V. Vartanian *et al.*, "Patterned Defect & CD Metrology by TSOM Beyond the 22 nm Node," Metrology, Inspection, and Process Control for Microlithography Xxvi, Pts 1 and 2, 8324, (2012).